Modeling microstructure formation in block copolymer membranes using dynamical self-consistent field theory

Douglas J. Grzetic,[*,†] Anthony J. Cooper,[*,‡] Kris T. Delaney,[*,†] and Glenn H. Fredrickson[*,†,¶]

†*Materials Research Laboratory, University of California, Santa Barbara, California 93106, USA*

‡*Department of Physics, University of California, Santa Barbara, California 93106, USA*

¶*Departments of Chemical Engineering and Materials, University of California, Santa Barbara, California 93106, USA*

E-mail: dgrzetic@mrl.ucsb.edu; acooper@ucsb.edu; kdelaney@mrl.ucsb.edu; ghf@ucsb.edu

Abstract

Block copolymers have attracted recent interest as candidate materials for ultrafiltration membranes, due to their ability to form isoporous integral-asymmetric membranes by the combined processes of self-assembly and nonsolvent-induced phase separation (SNIPS). However, the dependence of surface layer and substructure morphologies on the processing variables associated with SNIPS is not well understood, nor is the interplay between microphase and macrophase separation in block copolymers undergoing such coagulation. Here, we use dynamical self-consistent field theory to simulate the microstructure evolution of block copolymer films during SNIPS, and find that such films form the desired sponge-like asymmetric porous substructure only if the solvent

1

and nonsolvent have opposite block selectivities, and that otherwise they form a dense nonporous microphase separated film. Our results could have important implications for the choices of solvent and nonsolvent in the processing of block copolymer membranes.

Membrane technologies play a critical role in human health and quality of life, from applications such as desalination and waste water treatment,[1,2] bioseparations[3] and drug delivery,[4] to industrial liquid and gas separations[5] and fuel cells/batteries.[6,7] Polymer-based membranes play a prominent role in all of these areas, and are particularly ubiquitous in microfiltration (particle filtering in the range $10~\mu\text{m} - 100~\text{nm}$) and ultrafiltration ($100~\text{nm} - 10~\text{nm}$) membranes used for water purification applications.[8] Improving the effectiveness and cost-efficiency of this class of polymer membranes is key to increasing access to safe drinking water and mitigating human environmental impact across the globe. Toward this goal, we must improve our fundamental understanding of what constitutes an optimal polymer membrane structure for a given application, and how to fabricate such materials in an economical and industrially scalable way.

One of the most widely used types of polymer-based water filtration membranes are *integral-asymmetric* membranes.[8,9] This class of membranes has an asymmetric pore distribution consisting of small, highly selective pores near the membrane surface, which are mechanically supported by a more open porous substructure. The asymmetric pore structure ensures that the membrane achieves a high selectivity and mechanical strength without sacrificing the flux through the membrane. Such membranes are most often fabricated using a process called *nonsolvent-induced phase separation*, or NIPS, wherein a film of a homopolymer solution is cast and then immersed in a nonsolvent bath.[10,11] Mass transfer between the solvent and nonsolvent causes phase separation into polymer-lean and polymer-rich domains, which initiates at the film surface and propagates into the film. The polymer-rich domains ultimately vitrify or crystallize, which results in a kinetically-trapped structure that, under certain processing conditions, has the desired asymmetric pore distribution.

Decades of research, both experimental[11,12] and theoretical,[13–21] have attempted to elucidate the processing conditions that lead to an optimal asymmetric membrane via NIPS, but it is notoriously difficult to control the distribution and size dispersity of the pores at the surface layer, which largely determine the membrane's selectivity performance. An alternate approach, which has received growing interest in recent years, is to use *block copolymers* in place of homopolymers, to construct integral-asymmetric membranes that exploit the self-assembling properties of block copolymers to achieve a highly ordered *isoporous* surface layer. This involves treating the (block copolymer) casting solution with a solvent evaporation step prior to immersion in the nonsolvent bath, and the resulting self-assembly-plus-nonsolvent-induced phase separation process is referred to as SNIPS.[7,8,22] Using SNIPS, integral-asymmetric isoporous membranes have been fabricated that outperform their conventional homopolymer-based counterparts,[23,24] but there are still numerous challenges involved in making these membranes reliably and economically, preventing the adoption and scaling up of this approach in industry. An additional complication is that SNIPS shares all of the NIPS parameters (casting solution composition, polymer molecular weight, solvent choice) but also depends on the block copolymer chemistry and architecture, solvent and nonsolvent block selectivities, and the duration of the solvent evaporation step. This makes it crucial to develop theoretical and computational methods that can aid in screening candidate block copolymer chemistries, architectures, and solvents, optimize processing variables, and overall contribute to the fundamental understanding of SNIPS.

In this work, we present a theoretical model and simulation workflow for studying block copolymer membrane formation via SNIPS. Although SNIPS is technically a multi-stage process that involves an initial solvent evaporation step prior to the immersion in a nonsolvent bath, here we focus on simulating the latter nonsolvent-immersion stage. To account for the evaporation step, we construct a post-evaporation initial condition for the partially ordered film using equilibrium self-consistent field theory (SCFT), which we then feed into dynamical self-consistent field theory (DSCFT) to simulate the membrane's structural evo-

lution during nonsolvent immersion. Although in recent decades there have been numerous theoretical/numerical studies of both homopolymer membrane formation via NIPS [13–21] as well as solvent evaporation of block copolymer films, [25–30] this is to our knowledge the first attempt to construct a theoretical framework that can be used to systematically investigate how the structure of block copolymer membranes, formed during nonsolvent-induced phase separation, depends on thermodynamic and kinetic parameters. Figure 1 (right panel) shows an example of an initialized film-bath interface in 2D for an AB diblock copolymer (P) plus solvent (S) and nonsolvent (N) system, containing an ordered interfacial surface layer of thickness h, as well as the 1D SCFT density profile that is used to construct it. Details of this initialization, as well as our implementation of DSCFT, can be found in the Supporting Information.
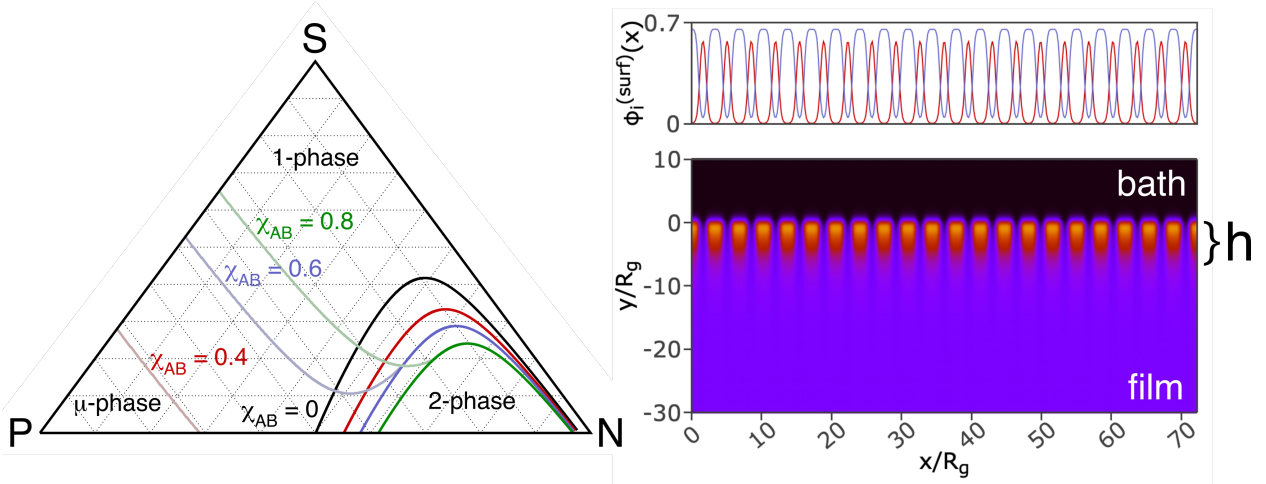

Figure 1: Left panel: ternary phase diagram for the block copolymer + solvent + nonsolvent system. The parameters $N_P = 50$, $f_A = 0.3$, $\chi_{AS} = \chi_{BS} = 0$, and $\chi_{AN} = \chi_{BN} = 1$ are fixed. Spinodals are shown for $\chi_{AB} = 0$ (black), $\chi_{AB} = 0.4$ (red), $\chi_{AB} = 0.6$ (blue), and $\chi_{AB} = 0.8$ (green). Spinodals corresponding to a macrophase or microphase instability are indicated as dark or light colors, respectively. Right panel: initialization of the ordered surface layer for block copolymer SNIPS simulations in 2D. The top plot shows the composition profile from equilibrium SCFT ($\phi_A(x)$ in red, $\phi_B(x)$ in blue), for $N_P = 50$, $f_A = 0.3$, $\chi_{AB} = 0.8$, $\chi_{AS} = 0.9$, $\chi_{BS} = 0.6$, $\chi_{AN} = 1$, $\chi_{BN} = 1.3$, $\phi_P = 0.6$, $\phi_S = 0.22$, $\phi_N = 0.18$. The bottom plot shows the initial profile $\phi_B(\mathbf{r})$ with surface layer patterned according to Eq. S6, with thickness $h \approx 3.5 R_g$.

We first consider how microphase separation affects the thermodynamics of the block

copolymer ternary blend, in the context of SNIPS. Like the homopolymer ternary blend, there is a two-phase window in the nonsolvent-rich region of the phase diagram due to the polymer-nonsolvent repulsion (χ_{AN}, χ_{BN}), but in the block copolymer case there is also a window of microphase separation in the polymer-rich region whose size depends on the A-B block repulsion χ_{AB}. Figure 1 shows the ternary phase diagram for a $P + S + N$ mixture with degree of polymerization $N_P = 50$, block fraction $f_A = 0.3$, and Flory parameters $\chi_{AS} = \chi_{BS} = 0$, and $\chi_{AN} = \chi_{BN} = 1$, where A and B refer to the minority and majority block components, respectively. The spinodals indicating homogeneous phase stability limits with respect to both microphase and macrophase separation are plotted for different values of χ_{AB} (for more details on the spinodal calculations used here and in Figure 2, see the Supporting Information). For the case $\chi_{AB} = 0$, the block copolymer is effectively a homopolymer when the solvent and nonsolvent are nonselective, so the microphase window vanishes but the two-phase window remains. As χ_{AB} increases, the microphase window appears and expands, while the polymer-rich side of the two-phase window retreats due to the free energy penalty associated with unfavorable AB contacts.

An important feature of the block copolymer ternary phase diagram is that the microphase spinodals are *not* at constant-ϕ_P (ϕ_i being the volume fraction of component i) when the AB symmetry is broken (if $f_A \neq 0.5$, $\chi_{AS} \neq \chi_{BS}$ or $\chi_{AN} \neq \chi_{BN}$). This can be seen in Figure 1 as an upturn of the microphase spinodal as it approaches the two-phase region. This feature is significant, because it allows the composition trajectory in SNIPS (which can be approximated by a constant-ϕ_P trajectory from the $\phi_N = 0$ axis to the $\phi_S = 0$ axis) to cross a microphase boundary before (or instead of) a macrophase boundary during the course of solvent-nonsolvent exchange. In this case SNIPS could result in the nonsolvent-induced propagation of an ordered microphase into the film, at least during the early stages, rather than generating the desired open porous substructure. It is thus crucial to understand the conditions under which this happens, and what its impact is on the membrane structure.

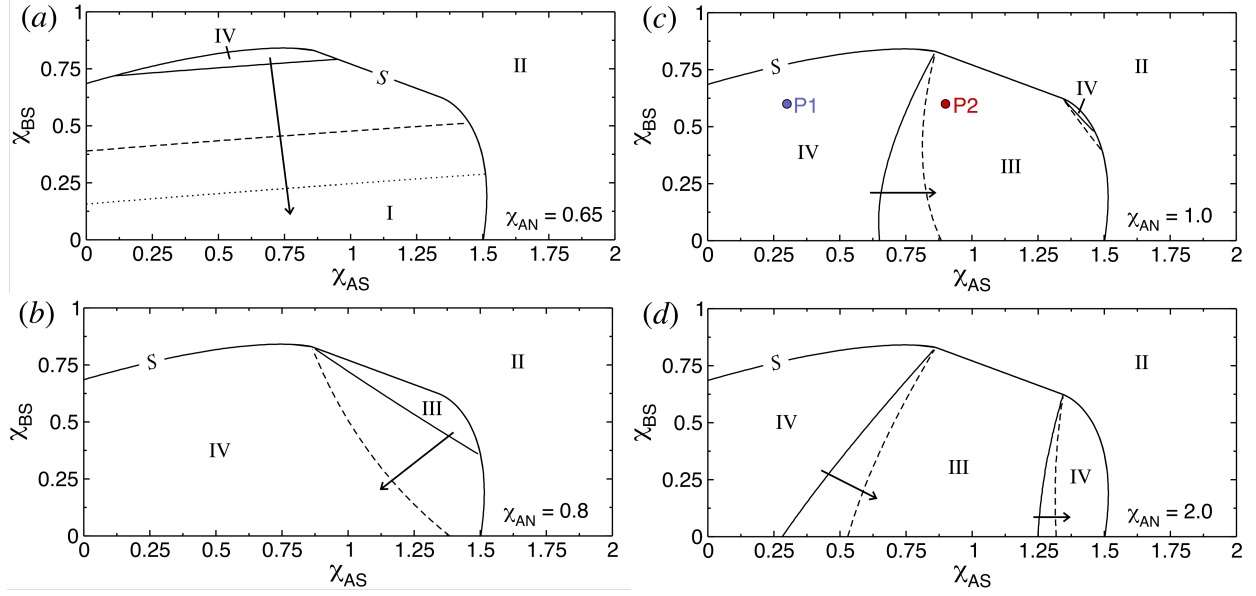For a film with a given polymer concentration ϕ_P, we can probe the nature of the SNIPS

Figure 2: Effect of solvent-polymer χ parameters (χ_{AS}, χ_{BS}) on the nature of the solvent-nonsolvent mass transfer-induced instability. The category of the instability in each region is indicated. Panel (a) corresponds to $\chi_{AN} = 0.65$, with $\chi_{BN}/\chi_{AN} = 1.29$ (solid), 1.3 (dashed), and 1.305 (dotted) shown. Panel (b) corresponds to $\chi_{AN} = 0.8$, with $\chi_{BN}/\chi_{AN} = 1.1$ (solid) and 1.3 (dashed) shown. Panel (c) corresponds to $\chi_{AN} = 1$, with $\chi_{BN}/\chi_{AN} = 1.1$ (solid) and 1.3 (dashed) shown, and also indicates the locations of systems $P1$ and $P2$, which are considered in Figure 3. Panel (d) corresponds to $\chi_{AN} = 2$, with $\chi_{BN}/\chi_{AN} = 1.1$ (solid) and 1.3 (dashed) shown. All cases correspond to $\phi_P = 0.2$, $\chi_{AB} = 0.8$, $N_P = 50$, $f_A = 0.3$, and the arrows indicate how the boundaries shift as χ_{BN}/χ_{AN} increases.

instability by tracing a linearly-interpolated mass-transfer trajectory from $\{\phi_S, \phi_N\} = \{1 - \phi_P, 0\}$ to $\{0, 1 - \phi_P\}$, and determining whether the resulting instability corresponds to a macrophase or a microphase. In general, a trajectory can be classified based on whether the system I) is stable along the entire trajectory, II) is already unstable in the absence of nonsolvent, III) first crosses a macrophase spinodal, or IV) first crosses a microphase spinodal along the trajectory. Using this classification, we can explore the phase space of solvent and non-solvent χ parameters and map out where in that space the different types of SNIPS instabilities occur. We will restrict ourselves to the case where the nonsolvent is selective for the A block $(\chi_{BN}/\chi_{AN} > 1)$, in order to mimic the preference of water for the polar (PEO or P4VP) minority block in experimental SNIPS.[8,9]

Figure 2 shows how the different regions of instability are affected by the solvent-polymer χ parameters $\{\chi_{AS}, \chi_{BS}\}$, for a system with $\phi_P = 0.2$, $N_P = 50$, $\chi_{AB} = 0.8$, and $f_A = 0.3$. In panels a, b, c, and d of Figure 2 we explore a range of increasing values of the block A-nonsolvent repulsion ($\chi_{AN} = 0.65$, 0.8, 1.0, and 2.0, respectively). Note that if χ_{AS} and/or χ_{BS} are sufficiently large, the solvent itself behaves as a nonsolvent, so all four panels contain a boundary $\mathcal{S}$ denoting the stability limit of the polymer-solvent film itself. As Figure 2a shows, if χ_{AN} and χ_{BN} are sufficiently small and the overall nonsolvent selectivity is weak $(\chi_{BN}/\chi_{AN} \lesssim 1.3)$, there is no SNIPS instability for any ϕ_N (labeled I). As χ_{BN}/χ_{AN} increases beyond roughly 1.3, however, the stable region is quickly replaced by a region of microphase instability (labeled IV). In all four panels, the arrow indicates the direction that a given boundary moves as the nonsolvent selectivity (χ_{BN}/χ_{AN}) is increased.

In Figure 2b the polymer-nonsolvent repulsion is sufficiently strong ($\chi_{AN} = 0.8$, $\chi_{BN} > 0.8$) that a macrophase window (labeled III) opens up, and grows as χ_{BN}/χ_{AN} increases from 1.1 to 1.3. The emergence of region III is important, because a macrophase instability is believed necessary to create the asymmetric porous underlayer in isoporous membranes. Note that this region lies entirely below the diagonal $(\chi_{BS} < \chi_{AS})$, meaning that in order to achieve a nonsolvent-induced macrophase instability the solvent should be selective for the

7

majority B block. Experimentally, casting solutions in SNIPS almost always (with a few exceptions[31,32]) contain two or more solvents with different block selectivities,[24,33–35] which limits our ability to quantitatively relate Figure 2 to the existing experimental literature. Nevertheless, the general principle is that a strong nonsolvent block selectivity provides a driving force for *microphase* separation in the film (region IV), and that this can be 'canceled out' by choosing a solvent with the opposite selectivity, leading to the desired nonsolvent-induced macrophase instability (region III). In Figures 2c and d, we increase the block A-nonsolvent repulsion ($\chi_{AN} = 1$ and 2, respectively), and find that although the macrophase separation window becomes larger, it remains located below the diagonal (where $\chi_{BS} < \chi_{AS}$).

In order to investigate how these thermodynamic considerations affect the evolution of the morphology in SNIPS, we now turn to dynamical SCFT simulations (DSCFT). We consider two systems with opposite solvent selectivities, labeled $P1$ and $P2$, for which $N_P = 50$, $f_A = 0.3$, $\chi_{AB} = 0.8$, $\chi_{AN} = 1$, $\chi_{BN} = 1.3$, where the initial film compositions in the bulk and at the surface layer of the film are $\{\phi_P, \phi_S, \phi_N\} = \{0.2, 0.62, 0.18\}$ and $\{0.6, 0.25, 0.15\}$, respectively. Both systems have $\chi_{BS} = 0.6$, but $P1$ has $\chi_{AS} = 0.3$ and $P2$ has $\chi_{AS} = 0.9$, placing $P1$ in region IV and $P2$ in region III (see Figure 2c). The ternary phase diagram in Figure 3b shows the spinodals corresponding to $P1$ (blue) and $P2$ (red), as well as the initial bulk film, surface layer, and bath compositions, and an arrow indicating the approximate composition trajectory expected in SNIPS.

In Figure 3a, we present a time series of the membrane morphologies in two dimensional DSCFT simulations of SNIPS, with times expressed in terms of the Rouse time τ_R.[36] The morphologies, described by the total polymer volume fraction ($\phi_P(\mathbf{r}) = \phi_A(\mathbf{r}) + \phi_B(\mathbf{r})$), are shown for systems $P1$ (top) and $P2$ (bottom). The simulations demonstrate that as nonsolvent diffuses into the film, these two systems develop dramatically different morphologies, that are qualitatively in line with our expectations from Figure 2. $P1$ develops a microphase separation front consisting of hexagonally-ordered micelles, that propagates into the film and shows no signature of macrophase separation at any point during the simulation. For $P2$,
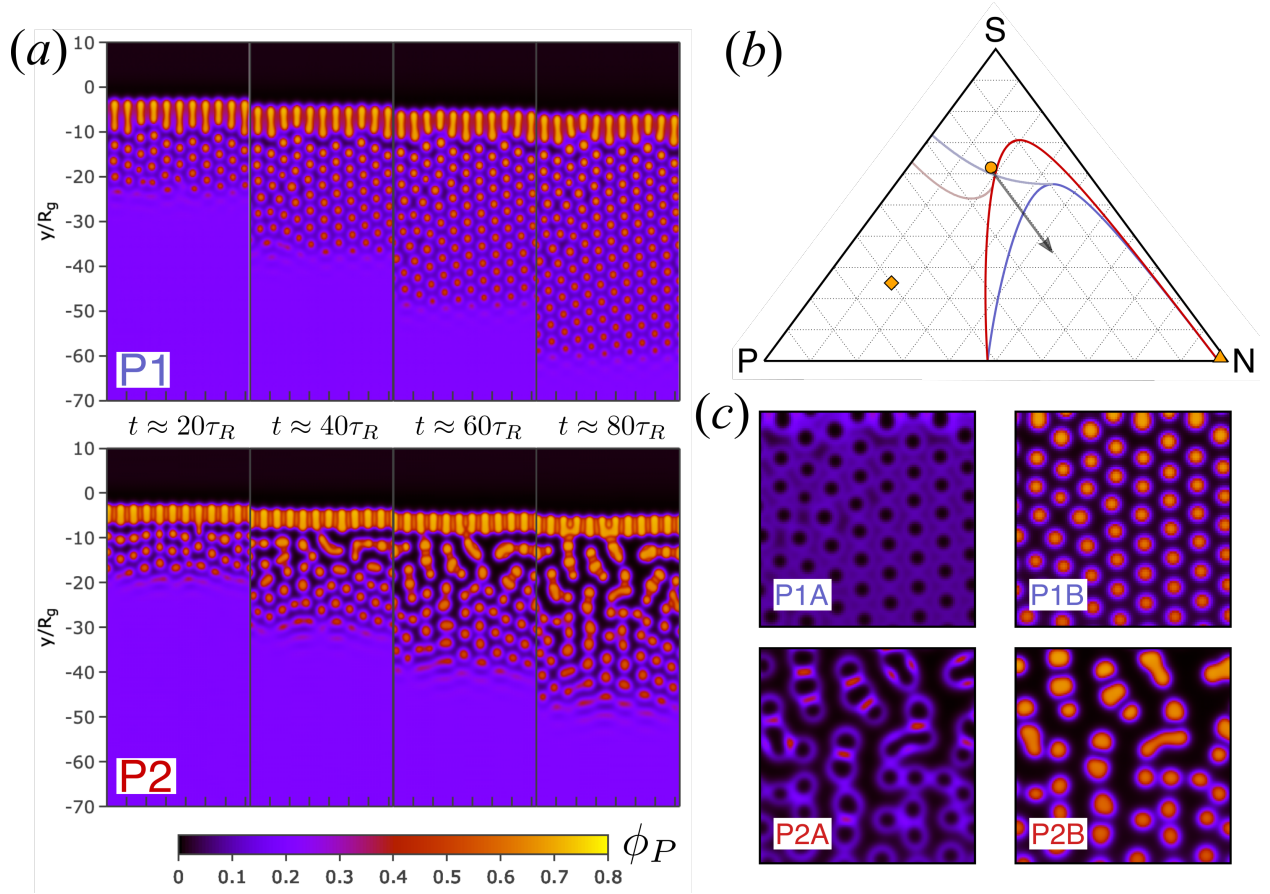
Figure 3: a) Morphology time series for systems $P1$ and $P2$, respectively, showing $\phi_P(\mathbf{r}, t) = \phi_A(\mathbf{r}, t) + \phi_B(\mathbf{r}, t)$ for times $t \approx 20\tau_R$, $40\tau_R$, $60\tau_R$ and $80\tau_R$. b) Ternary phase diagram corresponding to systems $P1$ (blue spinodals) and $P2$ (red spinodals). The orange circle denotes the initial bulk composition of the block copolymer film, the orange diamond denotes the initial composition of the surface layer, and the orange triangle denotes the initial composition of the nonsolvent bath. The arrow indicates the bulk film composition trajectory as it crosses the spinodal due to solvent-nonsolvent mass transfer. c) Density snapshots of polymer block A and block B for systems $P1$ and $P2$ just below the ordered surface layer, at time $t \approx 80\tau_R$.

the early stages look similar to $P1$ with the initial formation of micelles below the surface layer, but without the long-range order of the micelles in $P1$. Unlike $P1$, the later times clearly show macrophase separation of $P2$ into polymer-rich and polymer-poor domains.

Figure 3c shows zoomed-in snapshots of the morphologies of each block $\phi_A(\mathbf{r})$ and $\phi_B(\mathbf{r})$ for systems $P1$ and $P2$, beneath the ordered skin layer at $t \approx 80\tau_R$. Although species A forms the minority block, the micelle cores are in fact comprised of the majority B (PS) block, due to the strong selectivity of the nonsolvent for the A (PEO or P4VP) block. This leads to 'inverted' or so-called 'crew-cut' micelles in which the majority block forms a dense core that is surrounded by a lower density corona of the A block. In $P1$ these inverted micelles order into a hexagonally-packed arrangement, whereas in $P2$ they aggregate and are 'glued' together into clusters by the A block coronas, which themselves densify over time. The ability of block copolymers to form crew-cut micelles in selective solvents (particularly amphiphilic block copolymers in water) has been well established,[37,38] along with the tendency of those micelles to either assemble into ordered morphologies[38,39] or to aggregate and become trapped in complicated nonequilibrium structures such as helices of cylindrical micelles,[40,41] segmented cylindrical micelles,[41,42] or stringy "pearl necklace" aggregates[39,43] that resemble the structures shown in Figure 3.

It is generally understood that the casting solution contains micelles that order at the surface layer prior to the nonsolvent immersion step;[7–9] the consensus being that these are conventional micelles with cores comprised of the polar (minority) block.[9,33] This reasoning implies that the isoporous surface layer contains cylindrical hydrophilic pores, although there has been some debate about this.[24] Our results suggest the possibility that during SNIPS the conventional micelles in the casting solution invert into crew-cut micelles due to the strong interaction with the nonsolvent, and subsequently form aggregates as previously discussed. This idea is consistent with Ref. 33, in which it was demonstrated that mixtures of PS-b-P4VP block copolymer in THF/DMF formed micelles with P4VP cores, but upon the introduction of water formed micelles with PS cores, if allowed to equilibrate. However, for

this inversion to have time to occur in SNIPS, prior to the vitrification of the PS block, a slower rate of solvent-nonsolvent exchange than what is typically seen in SNIPS would probably be required.

Up to this point, our results have neglected the effects of polymer vitrification, but it is well known that such effects provide the dynamical arrest that is needed to stabilize the membrane structure.[7–9] In Figure 4a we present a late-time morphology snapshot of a DSCFT simulation corresponding to system $P2$ but which uses the viscous mobility model described in Eqns. S4 and S5, with a local relative viscosity for regions rich in species B given by $\gamma_B/\gamma_0 = 10^4$ and glass transition concentration (for the B block) of $\phi^* = 0.6$. In panel b of Figure 4 we show an equivalent morphology, at the same time, for the system without glass transition ($\gamma_B/\gamma_0 = 1$), for comparison. To the right of these morphology snapshots, their characteristic domain size is shown as a function of membrane depth, in units of the polymer radius of gyration R_g.[36]

The plots of domain size demonstrate the asymmetric nature of the membrane, as the ordered surface layer has a smaller characteristic domain size than the substructure beneath it. The simulation with glass transition exhibits an asymmetric pore distribution within the membrane substructure, with pore sizes that increase with depth up until the glass transition front. In contrast, the simulation without glass transition shows no obvious trend over the same range of depth (see the Supporting Information for a direct comparison). This glass transition-induced asymmetric pore distribution has been observed and explained already in Ref. 21 in the context of homopolymer NIPS membranes, but Figure 4 shows that a similar effect occurs in SNIPS, even when it is only the B block that vitrifies. The glass transition also helps to preserve the structure and alignment of the isoporous surface layer, as can be seen by comparing panels a and b.

Finally, in Figure 4c we show a series of membrane cross-sections obtained in 3D DSCFT simulations of system $P2$ (without glass transition). The 3D system allows initializing the proper isoporous surface layer with vertically oriented hexagonally-packed cylindrical pores,
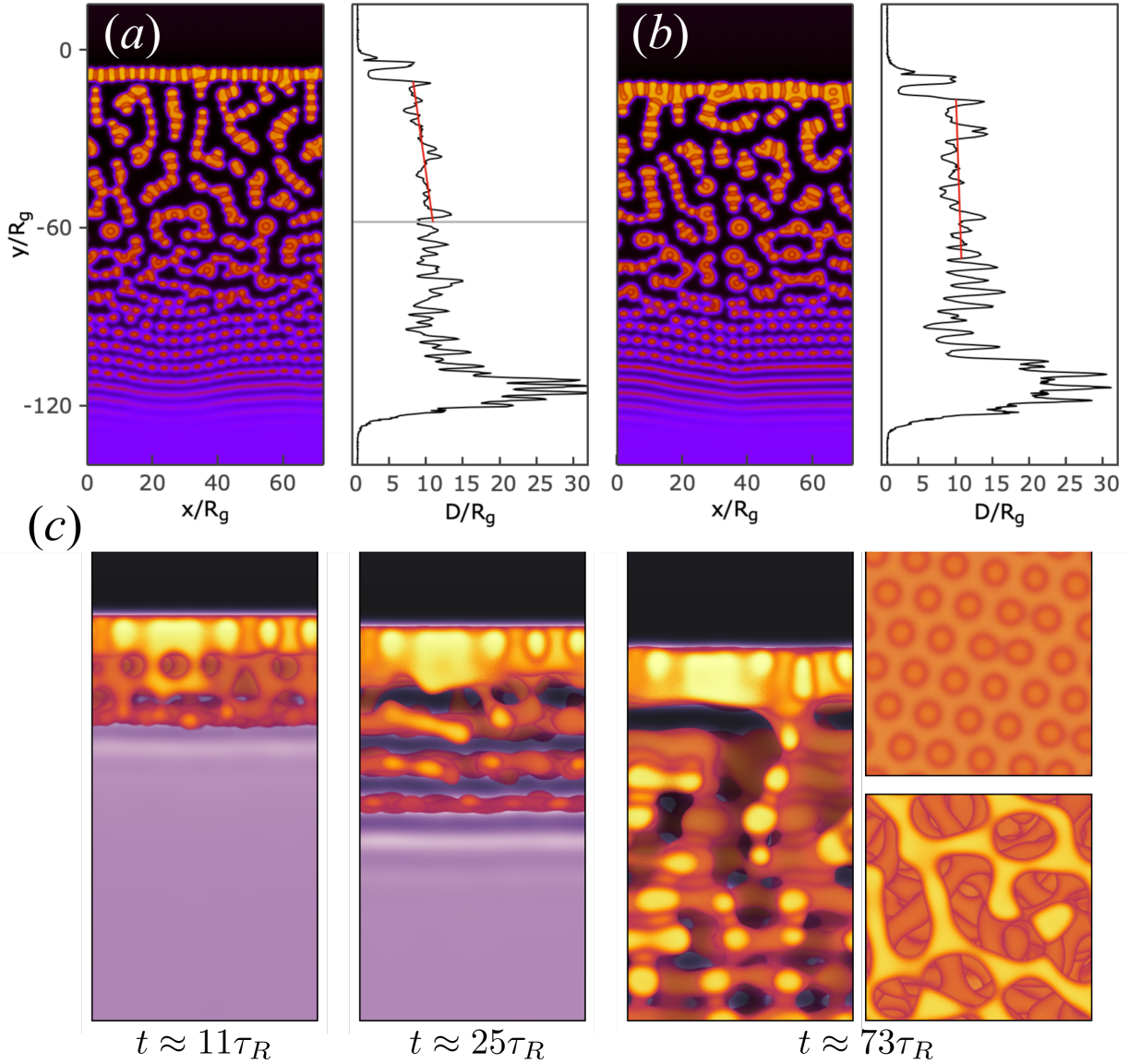
Figure 4: Morphologies corresponding to system $P2$, at time $t \approx 360\tau_R$, a) with glass transition, and b) without glass transition. The left panels in a) and b) show total polymer volume fraction ($\phi_P(\mathbf{r}) = \phi_A(\mathbf{r}) + \phi_B(\mathbf{r})$) morphology snapshots. The right panels of a) and b) show the characteristic domain size D/R_g as a function of depth in the film, and in a) the glass transition front is indicated as the horizontal grey line. Linear fits for both cases are shown as red lines. c) Morphology snapshots of total polymer volume fraction $\phi_P(\mathbf{r})$ from dynamical SCFT in 3D, corresponding to system $P2$ without glass transition, at times $t \approx 11\tau_R$ (left), $t \approx 25\tau_R$ (middle) and $t \approx 73\tau_R$ (right). The latest time shows membrane cross-section as well as views of the surface from above and substructure from below.

and demonstrates how the substructure forms by a layer-by-layer assembly of micelles into an interconnected network. Although our 2D results suggested that the polymer-rich domains in the substructure are not well connected, in 3D we can clearly see that they form an interconnected structure. For the latest time we also show views of the membrane surface from above and of the substructure from below, which demonstrate that the isoporous surface layer, containing cylindrical cores rich in the polar block,[44] remains stable, and that the sub-layer micelles are cylindrical.

In conclusion, we have presented an initial theoretical study of structure formation in block copolymer membranes during SNIPS. In addition to laying the groundwork for future investigations of SNIPS, our study reveals that the solvent and nonsolvent block selectivities play a critical role in determining the final membrane structure. We found that the desired morphology is obtained only when the solvent and nonsolvent have opposite block selectivities, otherwise a microphase instability is engaged during SNIPS, which is associated with an ordered micellar phase. Experimentally, this suggests using a solvent that is selective for the majority non-polar block, since water is usually the nonsolvent in SNIPS. In this work, we have focused primarily on exploring the solvent and nonsolvent χ parameters, and have only scratched the surface of the vast parameter space that is relevant for SNIPS. For example, exploring the role of the solvent-nonsolvent exchange rate, and the consideration of additional co-solvent species, will be important in future work to more realistically describe experimental SNIPS protocols. The thickness and composition of the ordered surface layer could also be treated as proxy variables for the solvent evaporation time, in lieu of a more sophisticated, explicit theoretical treatment[25–30] of the evaporation step. The incorporation of thermal fluctuations[21] and hydrodynamic effects[16,17,20] will also be important for future improvements to our model and workflow, which will enhance its ability to screen candidate polymer chemistries and architectures, solvent and nonsolvent selections, and help achieve process optimization in SNIPS.

Supporting Information Available

Acknowledgement

References

(1) Shannon, M. A.; Bohn, P. W.; Elimelech, M.; Georgiadis, J. G.; Marinas, B. J.; Mayes, A. M. Science and technology for water purification in the coming decades. *Nature* **2008**, *452*, 301–310.

(2) Werber, J. R.; Osuji, C. O.; Elimelech, M. Materials for next-Generation Desalination and Water Purification Membranes. *Nat. Rev. Mater.* **2016**, *1*, 16018.

(3) van Reis, R.; Zydney, A. Bioprocess membrane technology. *J. Membr. Sci.* **2007**, *297*, 16–50.

(4) Jackson, E. A.; Hillmyer, M. A. Nanoporous Membranes Derived from Block Copolymers: From Drug Delivery to Water Filtration. *ACS Nano* **2010**, *4*, 3548–3553.

(5) Rousseau, R. W., Ed. *Handbook of Separation Process Technology*; New York: Wiley, 1987; pp 862–964.

(6) Hallinan, D. T.; Balsara, N. P. Polymer Electrolytes. *Annu. Rev. Mater. Res.* **2013**, *43*, 503–525.

(7) Nunes, S. P. In *Sustainable Nanoscale Engineering*; Szekely, G., Livingston, A., Eds.; Elsevier, 2020; pp 297–316.

(8) Müller, M.; Abetz, V. Nonequilibrium Processes in Polymer Membrane Formation: Theory and Experiment. *Chem. Rev.* **2021**, *121*, 14189–14231.

(9) Hampu, N.; Werber, J. R.; Chan, W. Y.; Feinberg, E. C.; Hillmyer, M. A. Next-Generation Ultrafiltration Membranes Enabled by Block Polymers. *ACS Nano* **2020**, *14*, 16446–16471.

(10) Loeb, S.; Sourirajan, S. Sea Water Demineralization by Means of an Osmotic Membrane. *Adv. Chem. Ser.* **1963**, *38*, 117–132.

(11) Guillen, G. R.; Pan, Y.; Li, M.; Hoek, E. M. V. Preparation and Characterization of Membranes Formed by Nonsolvent Induced Phase Separation: A Review. *Ind. Eng. Chem. Res.* **2011**, *50*, 3798–3817.

(12) Wang, D.-M.; Lai, J.-Y. Recent advances in preparation and morphology control of polymeric membranes formed by nonsolvent induced phase separation. *Curr. Opin. Chem. Eng.* **2013**, *2*, 229–237.

(13) Cohen, C.; Tanny, G. B.; Prager, S. Diffusion-Controlled Formation of Porous Structures in Ternary Polymer Systems. *J. Polym. Sci., Polym. Phys. Ed.* **1979**, *17*, 477–489.

(14) Termonia, Y. Monte Carlo diffusion model of polymer coagulation. *Phys. Rev. Lett.* **1994**, *72*, 3678–3681.

(15) Zhou, B.; Powell, A. C. Phase field simulations of early stage structure formation during immersion precipitation of polymer membranes in 2D and 3D. *J. Membr. Sci.* **2006**, *268*, 150–164.

(16) Tree, D. R.; Delaney, K. T.; Ceniceros, H. D.; Iwama, T.; Fredrickson, G. H. A multi-fluid model for microstructure formation in polymer membranes. *Soft Matter* **2017**, *13*, 3013.

(17) Tree, D. R.; Iwama, T.; Delaney, K. T.; Lee, J.; Fredrickson, G. H. A multi-fluid model for microstructure formation in polymer membranes. *Soft Matter* **2017**, *13*, 3013.

(18) Hopp-Hirschler, M.; Nieken, U. Modeling of pore formation in phase inversion process: Model and numerical results. *J. Membr. Sci.* **2018**, *564*, 820–831.

(19) Lin, H.-H.; Tang, Y.-H.; Matsuyama, H.; Wang, X.-L. Dissipative particle dynamics simulation on the membrane formation of polymer-solvent system via nonsolvent induced phase separation. *J. Membr. Sci.* **2018**, *548*, 288–297.

(20) Tree, D. R.; aand C. B. Wilson, L. F. D. S.; Scott, T. R.; Garcia, J. U.; Fredrickson, G. H. Mass-transfer driven spinodal decomposition in a ternary polymer solution. *Soft Matter* **2019**, *15*, 4614–4628.

(21) Garcia, J. U.; Iwama, T.; Chan, E. Y.; Tree, D. R.; Delaney, K. T.; Fredrickson, G. H. Mechanisms of Asymmetric Membrane Formation in Nonsolvent-Induced Phase Separation. *ACS Macro Lett.* **2020**, *9*, 1617–1624.

(22) Radjabian, M.; Abetz, V. Advanced porous polymer membranes from self-assembling block copolymers. *Prog. Polym. Sci.* **2020**, *102*, 101219.

(23) Peinemann, K.-V.; Abetz, V.; Simon, P. F. W. Asymmetric superstructure formed in a block copolymer via phase separation. *Nat. Mater.* **2007**, *6*, 992–996.

(24) Nunes, S. P.; Sougrat, R.; Hooghan, B.; Anjum, D. H.; Behzad, A. R.; Zhao, L.; Pradeep, N.; Pinnau, I.; Vainio, U.; Peinemann, K.-V. Ultraporous Films with Uniform Nanochannels by Block Copolymer Micelles Assembly. *Macromolecules* **2010**, *43*, 8079–8085.

(25) Tsige, M.; Mattsson, T. R.; Grest, G. S. Morphology of Evaporated Multiblock Copolymer Membranes Studied by Molecular Dynamics Simulations. *Macromolecules* **2004**, *37*, 9132–9138.

(26) Marques, D. S.; Vainio, U.; Chaparro, N. M.; Calo, V. M.; Bezahd, A. R.; Pitera, J. W.; Peinemann, K.-V.; Nunes, S. P. Self-assembly in casting solutions of block copolymer membranes. *Soft Matter* **2013**, *9*, 5557.

(27) Paradiso, S. P.; Delaney, K. T.; Garcia-Cervera, C. J.; Ceniceros, H. D.; Fredrickson, G. H. Block Copolymer Self Assembly during Rapid Solvent Evaporation: Insights into Cylinder Growth and Stability. *ACS Macro Lett.* **2014**, *3*, 16–20.

(28) Berezkin, A. V.; Papadakis, C. M.; Potemkin, I. I. Vertical Domain Orientation in Cylinder-Forming Diblock Copolymer Films upon Solvent Vapor Annealing. *Macromolecules* **2016**, *49*, 415–424.

(29) Ibbeken, G. J. Self-Assembly of Polymers in Presence of Solvent Evaporation. Ph.D. thesis, Georg-August University, Göttingen, Germany, 2020.

(30) Dreyer, O.; Ibbeken, G.; Schneider, L.; Blagojevic, N.; Radjabian, M.; Abetz, V.; Müller, M. Simulation of Solvent Evaporation from a Diblock Copolymer Film: Orientation of the Cylindrical Mesophase. *Macromolecules* **2022**, *55*, 7564–7582.

(31) Hahn, J.; Clodt, J. I.; Abetz, C.; Filiz, V.; Abetz, V. Thin Isoporous Block Copolymer Membranes: It Is All about the Process. *ACS Appl. Mater. Interfaces* **2015**, *7*, 21130–21137.

(32) Bucher, T.; Filiz, V.; Abetz, C.; Abetz, V. Formation of Thin, Isoporous Block Copolymer Membranes by an Upscalable Profile Roller Coating Process-A Promising Way to Save Block Copolymer. *Membranes* **2018**, *8*.

(33) Oss-Ronen, L.; Schmidt, J.; Abetz, V.; Radulescu, A.; Cohen, Y.; Talmon, Y. Characterization of Block Copolymer Self-Assembly: From Solution to Nanoporous Membranes. *Macromolecules* **2012**, *45*, 9631–9642.

(34) Sutisna, B.; Polymeropoulos, G.; Musteata, V.; Peinemann, K.-V.; Avgeropoulos, A.; Smilgies, D.-M.; Hadjichristidis, N.; Nunes, S. P. Design of block copolymer membranes using segregation strength trend lines. *Mol. Syst. Des. Eng.* **2016**, *1*, 278.

(35) Phillip, W. A.; Dorin, R. M.; Werner, J.; Hoek, E. M. V.; Wiesner, U.; Elimelech, M. Tuning Structure and Properties of Graded Triblock Terpolymer-Based Mesoporous and Hybrid Films. *Nano Lett.* **2011**, *11*, 2892–2900.

(36) All lengths are given in units of $R_g = \sqrt{\frac{N_P}{6}} b$, and all times are given in units of the Rouse time $\tau_R = \frac{\zeta_0 N_P^2 b^2}{3\pi^2 k_B T}$, where ζ_0 is the monomeric friction coefficient, b is the statistical segment length and $k_B T$ is the thermal energy.

(37) Zhang, L.; Eisenberg, A. Multiple Morphologies of "Crew-Cut" Aggregates of Polystyrene-*b*-poly(acrylic acid) Block Copolymers. *Science* **1995**, *268*, 1728–1731.

(38) Zhang, L.; Eisenberg, A. Multiple Morphologies and Characteristics of "Crew-Cut" Micelle-like Aggregates of Polystyrene-*b*-poly(acrylic acid) Diblock Copolymers in Aqueous Solutions. *Science* **1995**, *268*, 1728–1731.

(39) Cameron, N. S.; Corbierre, M. K.; Eisenberg, A. 1998 E. W. R. Steacie Award Lecture Asymmetric amphiphilic block copolymers in solution: a morphological wonderland. *Can. J. Chem.* **1999**, *77*, 1311–1326.

(40) Dupont, J.; Liu, G. J.; Niihara, K.; Kimoto, R.; Jinnai, H. Self-Assembled ABC Triblock Copolymer Double and Triple Helices. *Angew. Chem., Int. Ed.* **2009**, *48*, 6144–6147.

(41) Hayward, R. C.; Pochan, D. J. Tailored Assemblies of Block Copolymers in Solution: It Is All about the Process. *Macromolecules* **2010**, *43*, 3577–3584.

(42) Zhu, J. T.; Jiang, W. Self-Assembly of ABC Triblock Copolymer into Giant Segmented Wormlike Micelles in Dilute Solution. *Macromolecules* **2005**, *38*, 9315–9323.

(43) Zhu, J. T.; Hayward, R. C. Spontaneous Generation of Amphiphilic Block Copolymer Micelles with Multiple Morphologies through Interfacial Instabilities. *J. Am. Chem. Soc.* **2008**, *130*, 7496–7502.

(44) Abetz, V. Isoporous Block Copolymer Membranes. *Macromol. Rapid Commun.* **2015**, *36*, 10–22.

TOC Graphic